Electronic Supplementary Information

Iron-doped ruthenium with good interfacial environment achieving superior hydrogen evolution activity under alkaline condition

Qun He,[‡,a] Yuzhu Zhou,[‡,a] Lihui Mou,[*,b] Chuanqiang Wu,[c] Daobin Liu,[b] Binghui Ge,[c] Jun Jiang,[*,b] and Li Song[*,a]

[a]National Synchrotron Radiation Laboratory, Free Electron Laser for Innovation Center of Energy Chemistry (FELiChEM), School of Nuclear Science and Technology, University of Science and Technology of China, Hefei 230029, China

bKey Laboratory of Precision and Intelligent Chemistry, Hefei National Research Center for Physical Sciences at the Microscale, School of Chemistry and Materials Science, University of Science and Technology of China, Hefei 230026, China

[c]Information Materials and Intelligent Sensing Laboratory of Anhui Province, Key Laboratory of Structure and Functional Regulation of Hybrid Materials of Ministry of Education, Institutes of Physical Science and Information Technology, Anhui University, Hefei 230601, China

E-mail: song2012@ustc.edu.cn; jiangj1@ustc.edu.cn; moulihui@ustc.edu.cn

[‡]These authors contributed equally to this work.

Experimental Section

Synthesis of RuFe/FeNC, RuFe/FeNC-high, RuFe/FeNC-low, Ru/FeNC and FeNC. All chemicals are of analytical grade and used as received. The typical procedure for synthesizing RuFe/FeNC involved dissolving 5 mL of pyrrole monomer, 0.02 mmol $RuCl_3 \cdot xH_2O$, and 0.005 mmol $FeCl_3 \cdot xH_2O$ in 100 mL of methanol to create a homogeneous solution. This solution was then stirred at room temperature for 24 hours to yield a uniform black suspension containing polypyrrole. Subsequent evaporation treatment at 80°C produced black powders as the precursor. The final sample was prepared by annealing the powder precursor at 750°C for 2 hours in an Ar atmosphere with a ramping rate of 2°C min^{-1}. The synthesis of RuFe/FeNC-high, RuFe/FeNC-low, FeNC followed a similar process to that of RuFe/FeNC, with the exception of the addition of 0.02 mmol $RuCl_3 \cdot xH_2O$, or change the molar numbers of $RuCl_3 \cdot xH_2O$ and $FeCl_3 \cdot xH_2O$ to 0.02 mmol/0.02 mmol and 0.02 mmol/0.0025 mmol, respectively. Ru/FeNC was synthesized using the following procedure: 50 mg of FeNC and 0.075 mmol $RuCl_3 \cdot xH_2O$ were dispersed in deionized water and stirred continuously. A dropwise addition of 0.15 mmol sodium borohydride ($NaBH_4$) solution (dispersed in 0.1 M KOH) was then made to reduce metal ions. After another 2 hours of stirring, the solid powder precursor was collected through successive vacuum filtration, deionized water washing, and overnight vacuum drying at 70°C. The final sample was obtained by annealing at 500°C for 1 hour in an Ar atmosphere to eliminate any potential residuals.

Characterization Methods. The structural properties of our samples were initially analyzed using X-ray diffraction (XRD) on a Rigaku SmartLab X-ray diffractometer. X-ray photoelectron spectroscopy (XPS) spectra were collected using a Thermo ESCALAB 250Xi spectrometer. The morphology and structure of the samples were examined through transmission electron microscopy (TEM) and high-resolution TEM (HRTEM) utilizing JEM-2100F field emission electron microscopy at an acceleration voltage of 200 kV. High-angle annular dark field scanning transmission electron microscopy (HAADF-STEM) was employed to observe atomic structures of the samples, conducted on a JEOL JEM-ARF200F (200 kV) equipped with a spherical aberration corrector. Elemental mapping was also quantified. Inductively coupled plasma-atomic emission spectroscopy (ICP-AES, PerkinElmer, Optima 7300 DV) was utilized to ascertain the metal loading quantities. Fe and Ru K-edge X-ray absorption fine structure (XAFS) spectra were gathered at beamline 1W1B of Beijing Synchrotron Radiation Facility (BSRF) and beamline BL14W1 of Shanghai Synchrotron Radiation Facility (SSRF).

Electrochemical Measurements. The electrochemical measurements were conducted using a CHI 760E electrochemical workstation (CH Instruments, China) with a standard three-electrode cell. This cell comprised a counter electrode (carbon rod), a working electrode (3 mm glassy carbon electrodes, GCE), and a reference electrode (Hg/HgO). The electrolyte employed was an Ar-saturated 1.0 M KOH solution. The preparation of the working electrode involved dispersing 4 mg of powder sample in a mixed solution of 0.40 mL H_2O, 0.55 mL isopropyl alcohol, and 0.05 mL 5% Nafion solution via sonication for two hours to yield a uniform ink. Subsequently, 2.5 μL or 5 μL (Pt/C) of this ink was drop-cast onto the GCE, which was then dried at room temperature. Prior to measurements, the reference electrode was calibrated using a hydrogen electrode (PHY-RHE). Cyclic voltammetry (CV) measurements were executed over 100 cycles (scan rate: 20 mV s^{-1}) to achieve stability. Linear sweep voltammetry (LSV) curves were subsequently recorded at a scan rate of 5 mV s^{-1}. Tafel slopes were derived by plotting potential (η) against log |j| from LSV curves. To assess electrochemical durability, chronoamperometry lines at an applied potential of -0.01 V vs. RHE and LSV curves after various CV cycles were collected. Electrochemical surface areas (ECSA) were evaluated through Cu underpotential deposition (UPD) and H adsorption/desorption processes. Intrinsic activity was then calculated based on ECSA, while mass activity was determined based on noble metal loading. TOF values were computed using the equation: TOF = I/2Fn, where I represents current (A), F denotes the Faraday constant (96485.3 C mol^{-1}), and n signifies the number of active sites (mol). The factor 1/2 accounts for the transfer of two electrons for one hydrogen molecule generation. n can be deduced from the charge accumulation (Q) of Cu deposition or H adsorption/desorption using the equation: n = Q/2F. All LSV curves were corrected with iR compensation.

In-Situ Raman and Synchrotron Radiation ATR-IR tests. Raman spectra were obtained In-situ using a WITec alpha 300R confocal Raman microscope equipped with a 600 grooves/mm diffraction grating. An exact power of 20 mW was applied to a 633 nm solid-state laser, serving as the excitation source. The calibration process utilized a silicon wafer standard at 520 cm^{-1}. A CCD featuring 1650x200 pixels was employed for spectral collection. Each Raman spectrum was acquired through ten scans. The potential range measured spanned from +0.06 V to -0.04 V relative to the RHE, maintaining a potential gap of 0.02 V. All electrochemical tests were conducted in an Ar-saturated 1.0 M KOH electrolyte solution.

In-situ synchrotron radiation ATR-IR analysis was conducted at the infrared beamline BL01B of Hefei Light Source (HLS), utilizing a Bruker vertex 80v FT-IR spectrometer, outfitted with an mercary-cadmium-telluride (MCT) detector that was cooled using liquid nitrogen. Both the catalyst and an IR reflective element were supported on an Au-coated Silicon conductive substrate. Each infrared absorption spectrum was obtained through 128 scans, each with a resolution of 4 cm^{-1}. Prior to each test, the background spectrum was collected at an open-circuit potential to correct the data. The measured potential range extended from +0.04 to -0.04 V relative to the RHE, with a potential gap of 0.02 V. All the electrochemical tests were conducted in an Ar-saturated 1.0 M KOH electrolyte.

AIMD Simulations and DFT Calculations. AIMD simulations were performed using the CP2K/Quickstep package.[1] The three-layer (4x4) supercell slabs with the bottom layer fixed were constructed and a vacuum layer of at least 20 Å was added. The interfacial water systems were modelled by introducing 36 water molecules onto the catalyst surfaces. The canonical ensemble condition (NVT) was imposed by a Nose-Hoover thermostat with a constant temperature of 300 K. The total simulation time was 20 ps to ensure the equilibration of interfacial water structures and the timestep was set to 1fs. DFT calculations using the one-layer-water model derived from the last snapshot of AIMD simulations were carried out via Vienna Ab-initio Simulation Package (VASP) package.[2] The projector-augmented wave (PAW) pseudopotential method[3] was used to describe the electron-ion interactions, and the Perdew-Burke-Ernzerhof (PBE)[4] functional within the generalized gradient approximation (GGA) framework[5] was used to determine the electron exchange-correlation interactions. Brillouin zone sampling was conducted using a Monkhorst Pack grid of 3x3x1 k-points. The cutoff energy was set at 500 eV and spin polarization was considered throughout the simulations. The zero-damping DFT-D3 method of Grimme[6] was introduced to calculate the van der Waals interactions. Ionic relaxation was converged until energy and force were reduced to within 1×10^{-5} eV and 0.02 eV/Angstrom, respectively. The transition state searches were conducted by combining the climbing image-nudged elastic band (CI-NEB) and dimer methods.[7] Vibrational frequencies were analyzed to confirm the transition state with only one imaginary frequency. The Gibbs free energy changes were evaluated according to $\Delta G=\Delta E+\Delta ZPE-T\Delta S$, where ΔZPE and ΔS are the changes in zero-point energy and entropy.

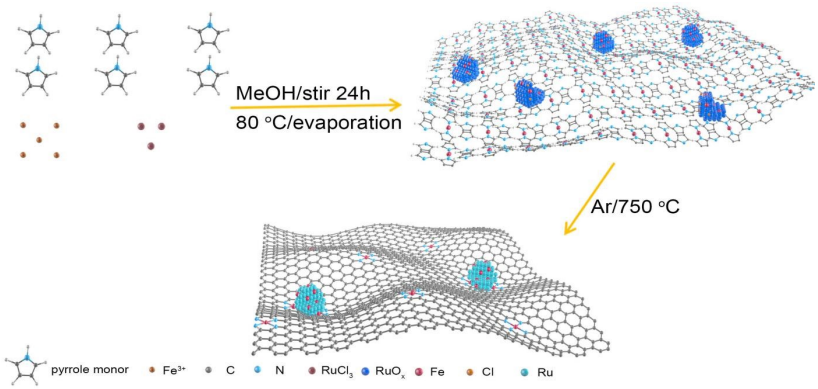

Fig. S1. Schematic synthesis process of RuFe/FeNC.

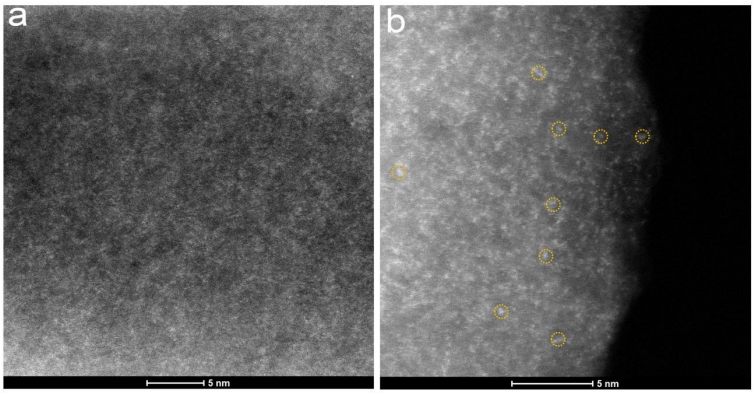

Fig. S2. HAADF-STEM images of (a) FeNC precursor and (b) RuFe/FeNC precursor.

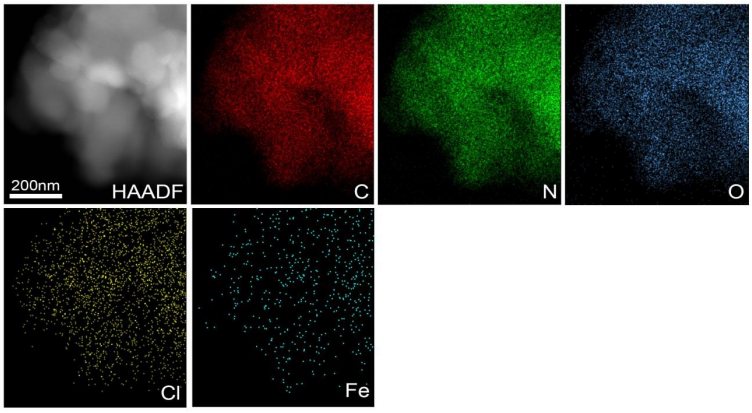

Fig. S3. Elemental mapping of FeNC precursor.

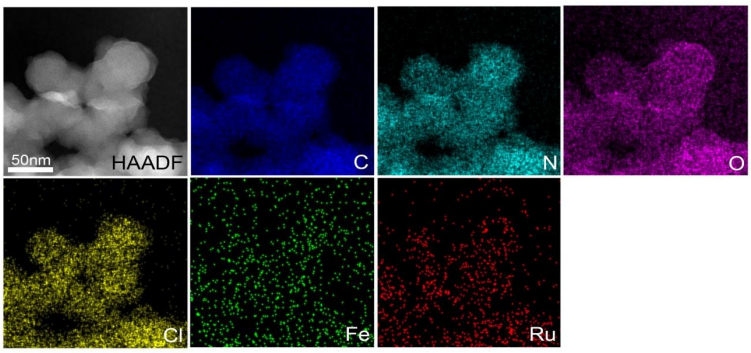

Fig. S4. Elemental mapping of RuFe/FeNC precursor.

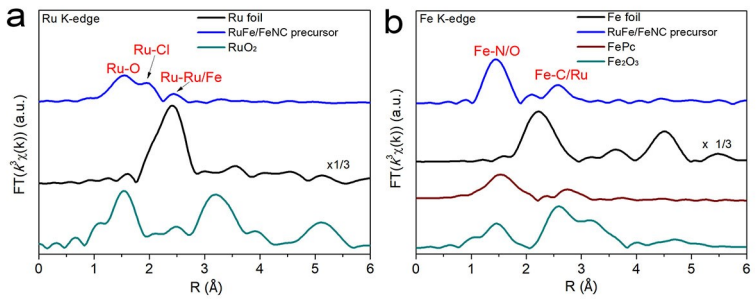

Fig. S5. (a) Ru K-edge FT-EXAFS spectra of RuFe/FeNC precursor and reference Ru foil, RuO_2. (b) Fe K-edge FT-EXAFS spectra of RuFe/FeNC precursor and reference Fe foil, FePc, and Fe_2O_3.

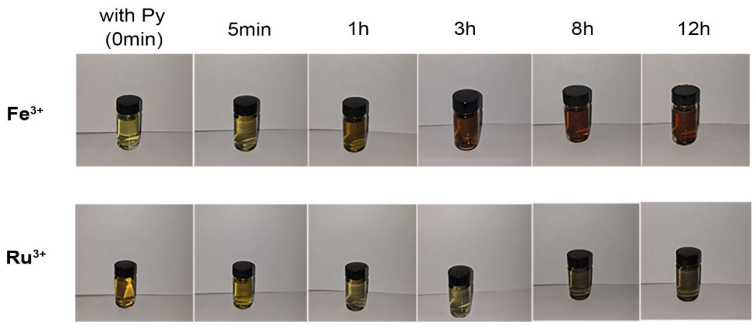

Fig. S6. A picture showing the polymerization process of pyrrole monomer catalyzed by different ions.

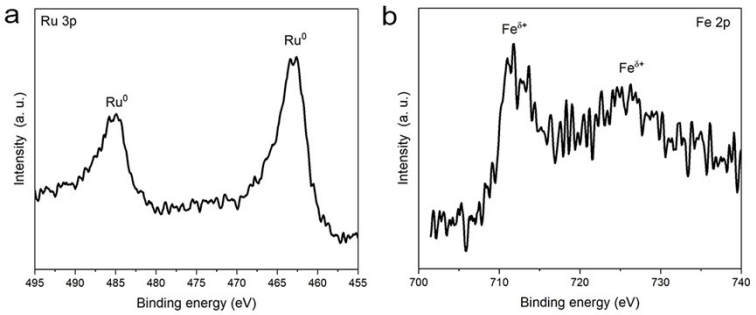

Fig. S7. (a) Ru 3p and (b) Fe 2p XPS results of Ru/FeNC.

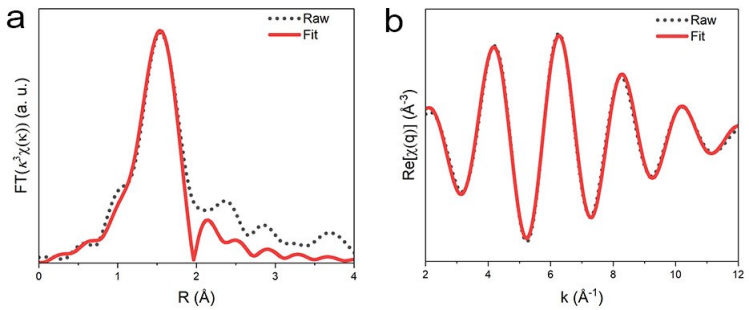

Fig. S8. FT-EXAFS and q-space fitting curves of FeNC.

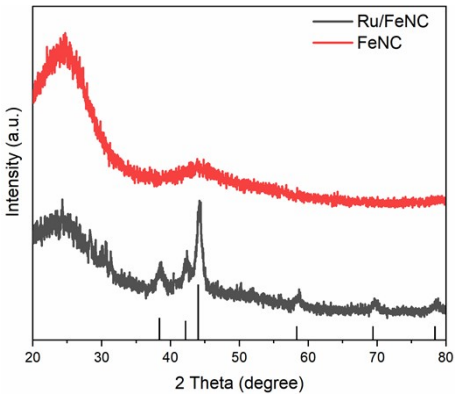

Fig. S9. XRD patterns of FeNC and Ru/FeNC.

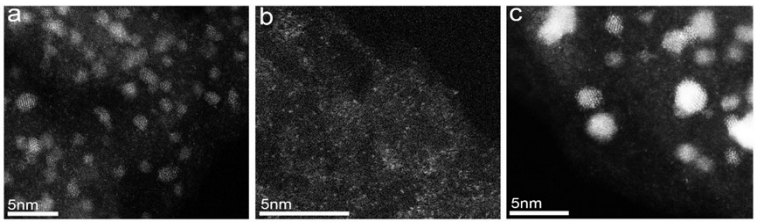

Fig. S10. HAADF-STEM images of (a) RuFe/FeNC, (b) FeNC, and (c) Ru/FeNC, respectively.

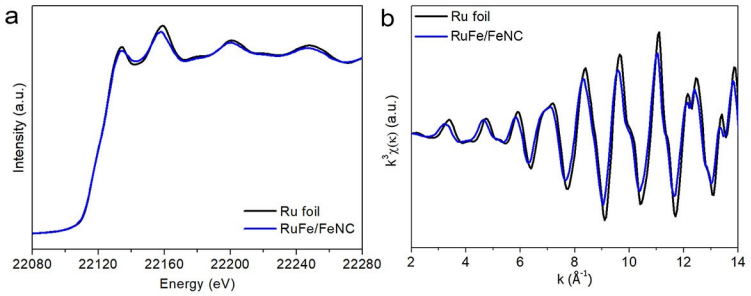

Fig. S11. (a) Ru K-edge XANES curves of Ru foil and RuFe/FeNC and (b) corresponding oscillation curves.

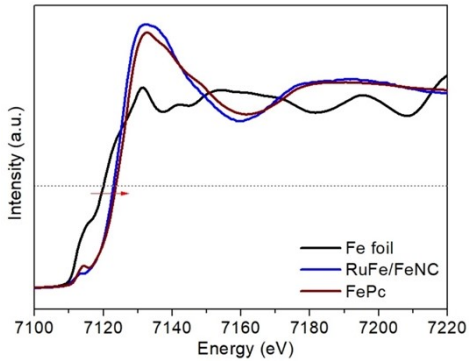

Fig. S12. Fe K-edge XANES curves of Fe foil, RuFe/FeNC and FePc.

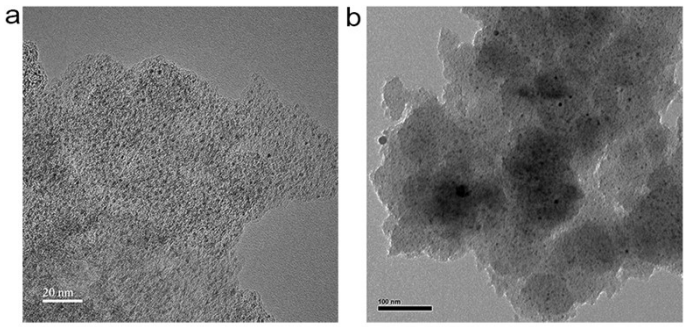

Fig. S13. TEM images of (a) RuFe/FeNC-low and (b) RuFe/FeNC-high.

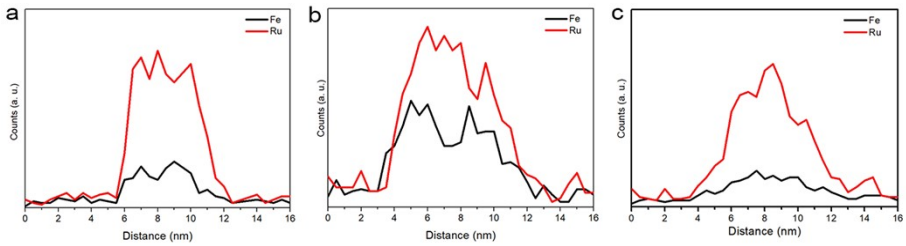

Fig. S14. Line scan profiles (a) RuFe/FeNC, (b) RuFe/FeNC-high and (c) RuFe/FeNC-low, respectively.

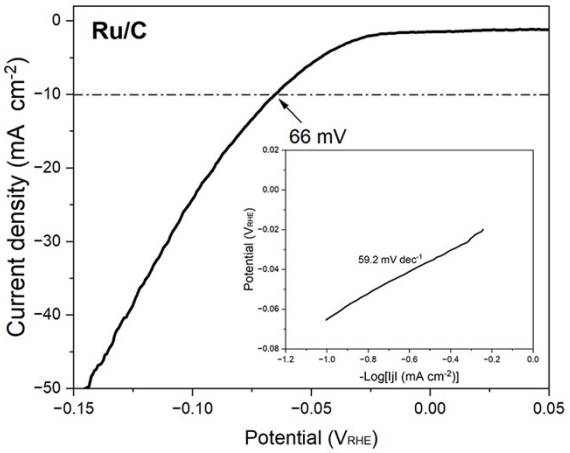

Fig. S15. LSV curve and Tafel slope of Ru/C recorded in 1.0 M KOH.

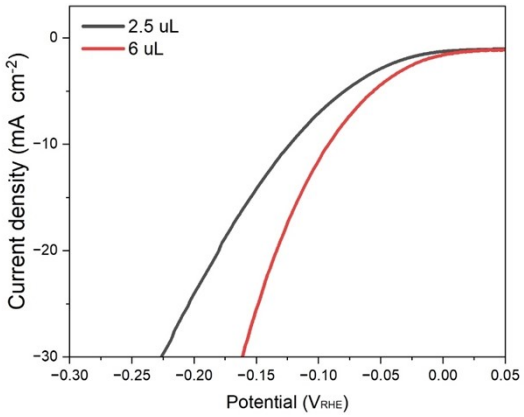

Fig. S16. LSV curves of Ru/FeNC in 1.0 M KOH with different ink loading.

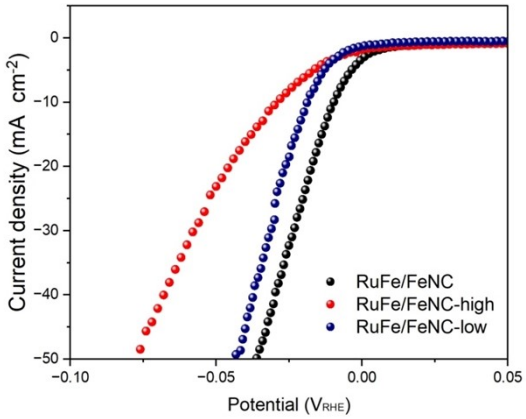

Fig. S17. LSV curves of RuFe/FeNC, RuFe/FeNC-low and RuFe/FeNC-high in 1.0 M KOH.

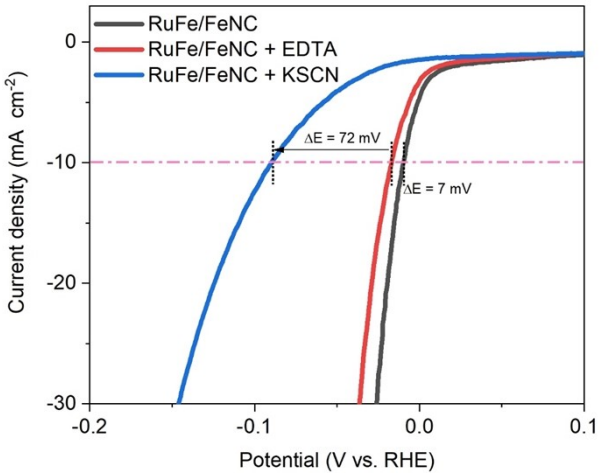

Fig. S18. KSCN and EDTA poison evaluation of RuFe/FeNC in 1.0 M KOH.

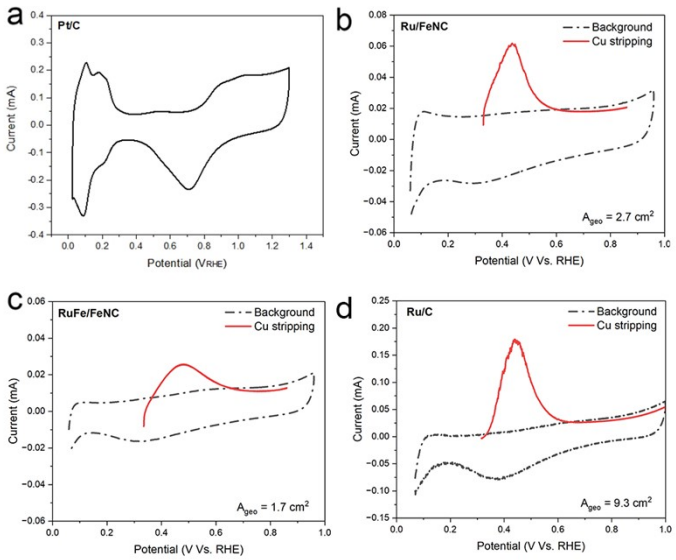

Fig. S19. (a) H adsorption/desorption curves on 20% Pt/C. (b,c) Cu UPD curves on Ru/FeNC and RuFe/FeNC in 0.05M H_2SO_4.

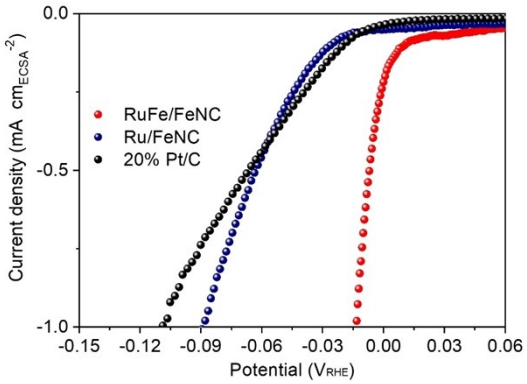

Fig. S20. ECSA-normalized LSV curves for 20% Pt/C, RuFe/FeNC and Ru/FeNC.

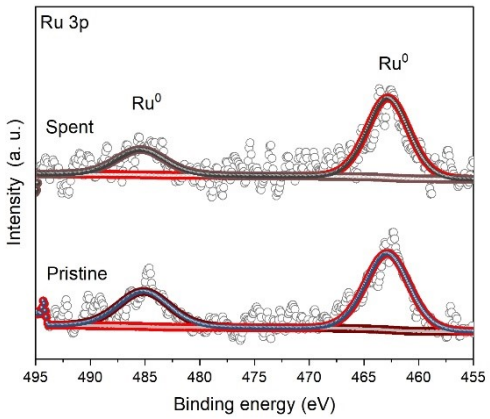

Fig. S21. Ru 3p XPS results of pristine and spent RuFe/FeNC.

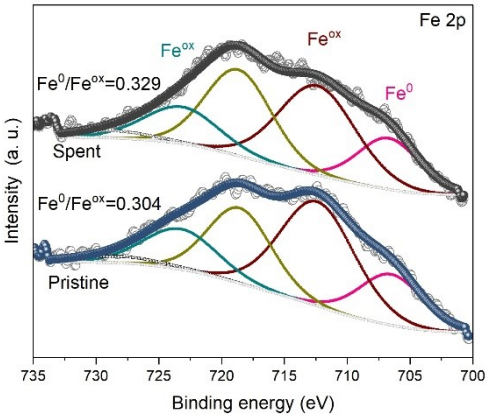

Fig. S22. Fe 2p XPS results of pristine and spent RuFe/FeNC.

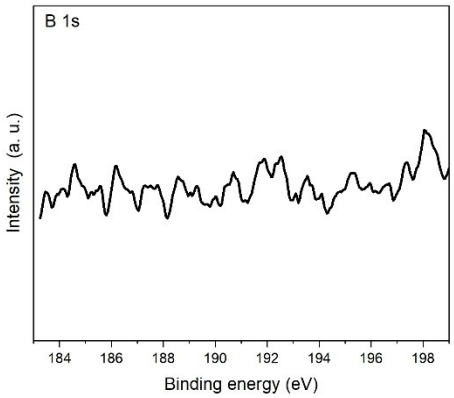

Fig. S23. B 1s XPS result of RuFe/FeNC.

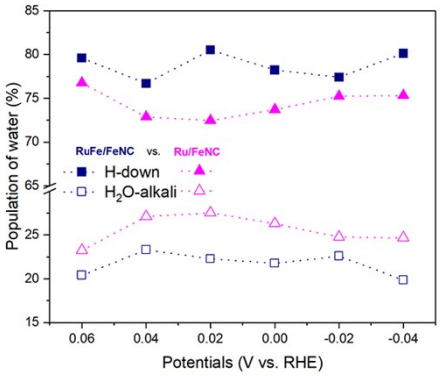

Fig. S24. Detailed intensity comparison of H-down and H_2O-alkali interfacial water molecules for both RuFe/FeNC and Ru/FeNC.

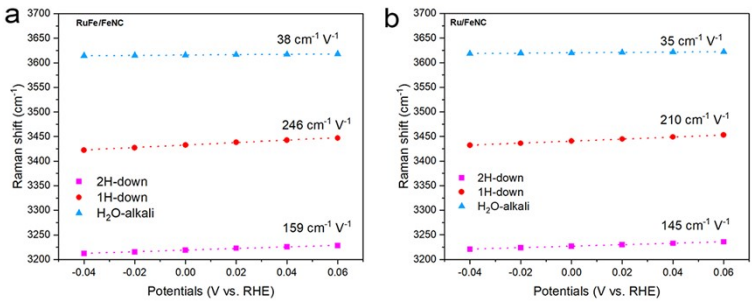

Fig. S25. The vibrational Stark effect induced Raman shifts as a function of potential for (a) RuFe/FeNC and (b) Ru/FeNC, respectively.

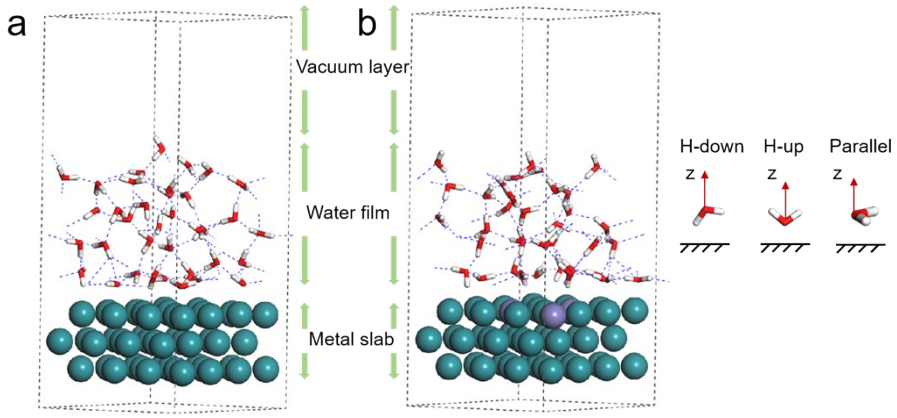

Fig. S26. Theoretical models of interfacial water over Ru and RuFe surfaces for AIMD simulations. Color code: Ru, dark green; Fe, purple; H, white; O, red. The blue dashed lines represent the hydrogen bond network.

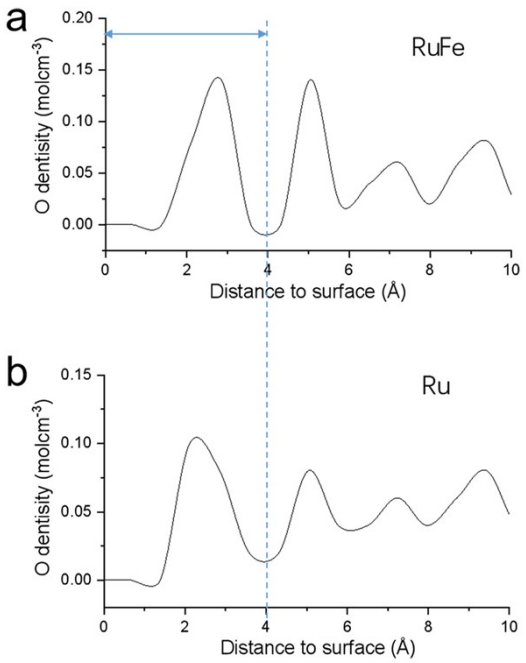

Fig. S27. The distribution density of oxygen along the Z direction analyzed by AIMD.

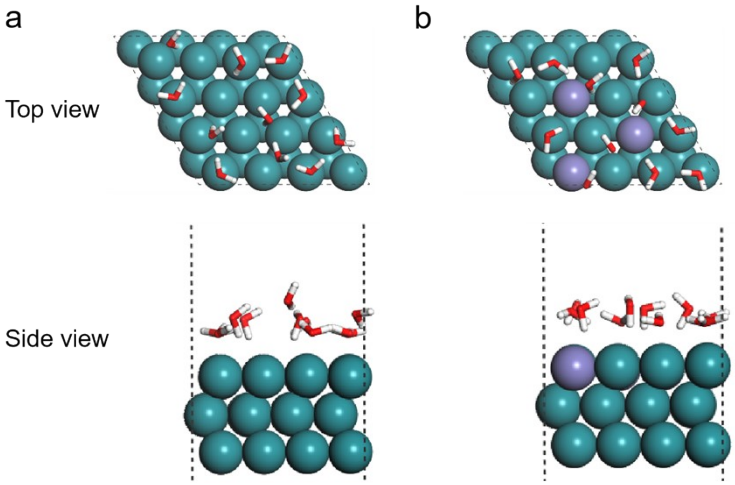

Fig. S28. Top and side views of one-layer-water models on (a) Ru and (b) RuFe surfaces for DFT calculations of HER. The initial structures were obtained from the last frame of a 20 ps AIMD simulation. The water layer is shown in stick mode. The dashed black line indicates the (4x4) simulation cell. Color code: Ru, dark green; Fe, purple; H, white; O, red.

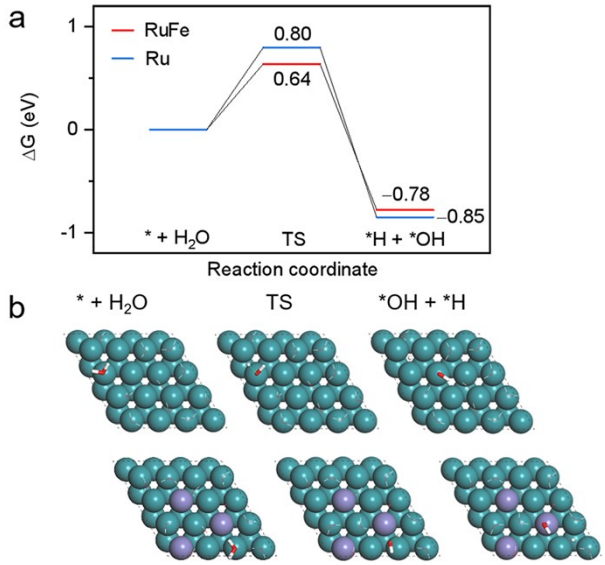

Fig. S29. (a) Gibbs free energy diagram of the parallel water dissociation on pure Ru and RuFe. (b) structures of reactant (* + H_2O), transition state (TS), and product (*OH + *H) of water dissociation step. The water molecule having the dissociation reaction is shown in stick mode, and the broken O-H bond is highlighted in green. Color code: Ru, dark green; Fe, purple; H, white; O, red.

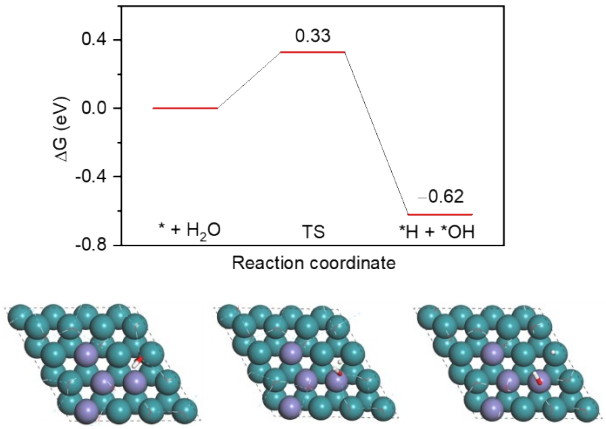

Fig. S30. Gibbs free energy diagram of water dissociation on Fe_4Ru and corresponding structures of reactant (* + H_2O), transition state (TS), and product (*OH + *H). The water molecule having the dissociation reaction is shown in stick mode, and the broken O-H bond is highlighted in green. Color code: Ru, dark green; Fe, purple; H, white; O, red.

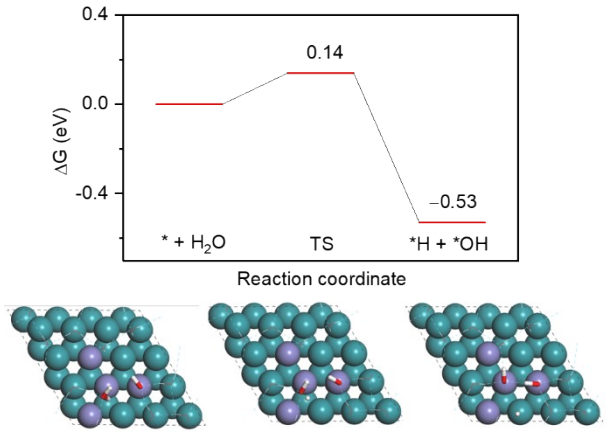

Fig. S31. Gibbs free energy diagram of water dissociation on Fe_4Ru with a OH ligand and corresponding structures of reactant (* + H_2O), transition state (TS), and product (*OH + *H). The water molecule having the dissociation reaction and the OH ligand are shown in stick mode, and the broken O-H bond is highlighted in green. Color code: Ru, dark green; Fe, purple; H, white; O, red.

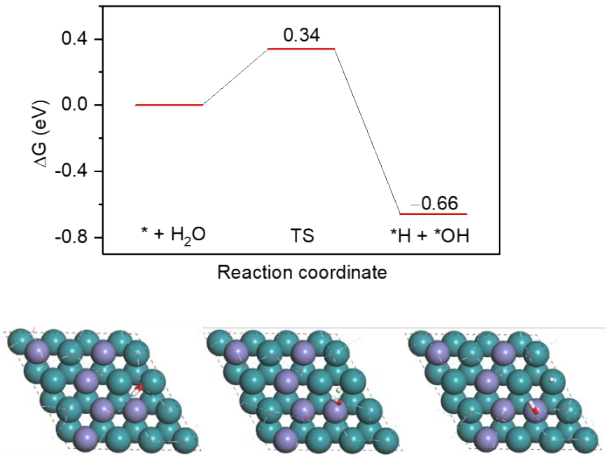

Fig. S32. Gibbs free energy diagram of water dissociation on Fe_6Ru and corresponding structures of reactant (* + H_2O), transition state (TS), and product (*OH + *H). The water molecule having the dissociation reaction is shown in stick mode, and the broken O-H bond is highlighted in green. Color code: Ru, dark green; Fe, purple; H, white; O, red.

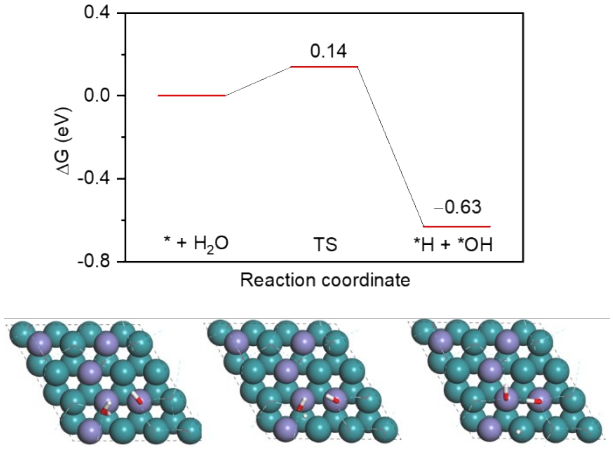

Fig. S33. Gibbs free energy diagram of water dissociation on Fe_6Ru with a OH ligand and corresponding structures of reactant (* + H_2O), transition state (TS), and product (*OH + *H). The water molecule having the dissociation reaction and the OH ligand are shown in stick mode, and the broken O-H bond is highlighted in green. Color code: Ru, dark green; Fe, purple; H, white; O, red.

Table S1. EXAFS fitting data of FeNC.

Sample	Path	N	R(Å)	σ^2 (10^{-3}Å^2)	Abs (ΔE_0) (eV)	R factor
FeNC	Fe-N	4.39±0.65	2.02	8.61	0.748	0.0047

Table S2. The Ru and Fe contents in RuFe/FeNC, Ru/FeNC, RuFe/FeNC-high and RuFe/FeNC-low determined by ICP-AES.

Sample	Mass ratio of Ru (%)	Mass ratio of Fe (%)
RuFe/FeNC	7.1	1.0
Ru/FeNC	15.3	0.8
RuFe/FeNC-high	7.3	2.6
RuFe/FeNC-low	7.6	0.6

Supplementary References

[1] J. VandeVondele, M. Krack, F. Mohamed, M. Parrinello, T. Chassaing, J. Hutter, *Comput. Phys. Commun.* 2005, 167, 103-128.

[2] G. Kresse, J. Furthmüller, *Phys. Rev. B* 1996, 54, 11169-11186.

[3] P. E. Blöchl, *Phys. Rev. B* 1994, 50, 17953-17979.

[4] J. P. Perdew, M. Ernzerhof, K. Burke, *J. Chem. Phys.* 1996, 105, 9982-9985.

[5] J. P. Perdew, K. Burke, M. Ernzerhof, *Phys. Rev. Lett.* 1996, 77, 3865-3868.

[6] S. Grimme, J. Antony, S. Ehrlich, H. Krieg, *J. Chem. Phys.* 2010, 132, 154104.

[7] G. Henkelman, H. Jónsson, *J. Chem. Phys.* 2000, 113, 9978-9985.